




**Coexisting orbits and chaotic dynamics of a confined self-propelled particle**Rubens H. Damascena , Leonardo R. E. Cabral , and Clécio C. de Souza Silva <sup>\*</sup>*Departamento de Física, Universidade Federal de Pernambuco, Cidade Universitária, 50670-901, Recife-PE, Brazil*

(Received 11 April 2022; accepted 7 June 2022; published 23 June 2022)

We investigate theoretically the dynamics of a confined active swimmer with velocity and orientation axis coupled to each other via a self-alignment torque. For an isotropic harmonic potential, this system is known to exhibit two distinct dynamical phases: a climbing one, where the particle is oriented radially and undergoes angular Brownian motion, and a circularly orbiting phase. Here we show that for nonradially symmetric confinement an assortment of complex phenomena emerge. For an elliptic harmonic potential the orbiting phase splits into several periodic orbits with a diversity of shapes: ovals, lemniscates, and generalized lemniscates with multiple lobes. These orbits can coexist in the parameter space and decay into one another induced by noise. For anharmonic confining potentials, we report transitions from periodic to chaotic dynamics, as one changes the intensity of the self-alignment torque and noise-induced complex orbits. These results demonstrate that the combination of the shape of the trapping potential and self-alignment torque can induce a rich variety of nontrivial dynamical states of a confined active particle.

DOI: [10.1103/PhysRevE.105.064608](https://doi.org/10.1103/PhysRevE.105.064608)**I. INTRODUCTION**

Self-propelled particles are nonequilibrium systems capable of converting energy absorbed from the environment into directed motion. They have been used as model systems to study complex behavior commonly observed in living systems, active colloids, vibrating grains, and self-propelled automated devices [1–9]. Unveiling their dynamical properties has led to crucial developments in the understanding of active matter and the wealth of associated phenomena [10–12].

Recently, there has been increasing interest on the properties of active particles interacting with boundaries or external potentials. For one thing, the confinement provides a means of measuring the intrinsic nonthermal pressure induced by the active matter and the force it produces on macroscopic objects [13–17]. For another, these systems allow one to probe statistical properties of active swimmers, such as steady-state probability distribution functions [18,19] and first passage times [20–23], that might distinguish them from passive Brownian particles. Last, the identification of novel dynamical phases of a confined active particle is of particular interest. Perrard *et al.* [24] has detected a variety of stable orbits in the motion of a harmonically confined magnetic droplet coupled to a vertically vibrating bath. Similar orbits were also identified in the problem of a circle swimmer with time-dependent propulsion in a static harmonic potential [25]. In both these examples, time dependence, of either the external potential or the self-propulsion, is a key ingredient for the observation of orbital motion.

In contrast to the above, the deterministic dynamics of an active particle confined in a static potential is rather simple:

The particle climbs uphill until its propulsion balances the force induced by the potential and it comes to rest. However, as recently shown by Dauchot and Démery [26], the situation changes dramatically when one considers the self-alignment dynamics of the particle axis toward its velocity vector. In this case, for sufficiently strong self-alignment torque, the climbing phase becomes unstable giving place to circular orbits. Another mechanism for orbital motion of active objects has been recently demonstrated in experiments performed on strongly confined walkers and surfers [27]. The authors attributed the observed dynamical phases to the interplay of active noise, strong confinement, and strong linear and angular inertial effects present in the investigated systems. These works suggest that the motion of a walker or swimmer in static confining potentials can be much more complex than previously thought. It is unclear, however, what kinds of orbits are possible when other confining potentials are considered. In particular, the possibility of chaotic orbits in these systems remains to be investigated.

In the present work, we investigate the dynamics of an overdamped active particle with self-alignment torque trapped in confining potentials of different shapes. By a detailed stability analysis of the fixed points of the system in the zero-noise limit, we show that the orbital motion is accessible in the parameter space for any shape of the confining potential. To investigate in detail the possible orbiting phases, we performed a series of numerical simulations, covering a wide range of the control parameters of different confining potentials. Our numerical results show that, on breaking the circular symmetry of the confining potential, a whole new world of dynamical phases and transitions between them emerges. For the noise-free case, the dynamical phase diagram typically features a sequence of distinct orbital phases characterized by different topological properties. In addition, in some regions of the parameter space, multiple periodic orbits can appear in

<sup>\*</sup>clecio.cssilva@ufpe.br

coexistence and decay into one another induced by noise. For certain types of anharmonic confining potential, we have also observed transitions from perfectly periodic to chaotic orbits, either induced deterministically, by a change in one of the system parameters, or stochastically, by small but sufficiently strong noise.

The paper is organized as follows. In Sec. II we introduce the model and discuss the relevant timescales of the problem. In Sec. III we present some general analytical results for arbitrary shapes of the confining potentials in the zero-noise limit and establish the conditions for the observation of orbital phases of the active particle. In Sec. IV we present numerical results describing different kinds of orbital motion in the noiseless regime for both harmonic and anharmonic confinements. The effects of noise are discussed in Sec. V. Finally, the conclusions and outlook are given in Sec. VI.

## II. MODEL DETAILS

### A. Equations of motion

We consider an overdamped self-propelled particle in two dimensions with position  $\mathbf{r} = (x, y)$  and orientation vector  $\hat{\mathbf{n}} = (\cos \theta, \sin \theta)$  trapped by a confining potential  $V(\mathbf{r})$ . The system dynamics is modeled by the following equations:

$$\dot{\mathbf{r}} = v_0 \hat{\mathbf{n}} - \mu \nabla V(\mathbf{r}), \quad (1)$$

$$\dot{\theta} = \beta (\hat{\mathbf{n}} \times \dot{\mathbf{r}}) \cdot \hat{\mathbf{z}} + \sqrt{2D} \xi(t), \quad (2)$$

where  $\mu$  is the translational mobility,  $v_0$  is the propulsion speed (thereby  $v_0/\mu$  is the propelling force intensity),  $D$  is the rotational diffusion constant, and  $\xi(t)$  is a white Gaussian noise with correlation  $\langle \xi(t) \xi(t') \rangle = \delta(t - t')$ . The first term in the right-hand side of Eq. (2) describes a restoring torque, which tends to align the particle orientation axis  $\hat{\mathbf{n}}$  with the center-of-mass velocity  $\mathbf{v} = \dot{\mathbf{r}}$ ,  $\hat{\mathbf{z}}$  being the rotation axis perpendicular to the  $xy$  plane [26,28]. The parameter  $\beta$  is a measure of how fast  $\hat{\mathbf{n}}$  relaxes toward  $\mathbf{v}$ . For  $\beta = 0$ , one recovers the standard model describing active Brownian particles (ABP) [10,11,29]. Notice that the self-alignment term is innocuous for a freely moving active particle, since in this case, from Eq. (1),  $\mathbf{v}$  and  $\hat{\mathbf{n}}$  are always parallel to each other. In the presence of an external force, however,  $\mathbf{v}$  and  $\hat{\mathbf{n}}$  are in general misaligned and the self-alignment term models, in a minimalist way, the tendency of these vectors to become parallel again.

Self-alignment dynamics similar to that described by Eq. (2) have been used to successfully model crawling cells [1,2,30,31], self-propelled hard disks [28,32,33], and a self-propelled robot in a harmonic trap [26]. As argued in Ref. [26], this term can also be relevant for other active systems, including, for example, spherical Janus colloids, where the left-right symmetry of the moving particle is broken every time  $\hat{\mathbf{n}}$  and  $\mathbf{v}$  are misaligned. In this case, a self-alignment torque could act to restore the symmetry.

### B. Timescales and nondimensionalization

The possible dynamical states emerging from any stochastic dynamical system is highly influenced by the interplay between the different timescales of the problem. The system

described by Eqs. (1) and (2) has three relevant timescales, which we will refer to as the *climbing time* ( $\tau_{cl}$ ), the *thermal reorientation time* ( $\tau_{th}$ ), and the *self-alignment time* ( $\tau$ ). The climbing time is the typical time the particle would take to climb the potential the furthest allowed by its propulsion in the absence of restoring torque and noise, that is,  $\tau_{cl} \sim \tau_0 \equiv L_0/v_0$ , where  $L_0$  is the distance between the origin and a point of the confining potential where  $|\nabla V| = v_0/\mu$ . The thermal reorientation time is a measure of how fast the particle orientation decorrelates due to thermal noise, that is,  $\tau_{th} \sim 1/D$  [29]. For  $\tau_{th} \ll \tau_0$ , the particle undergoes many thermal reorientations and thereby decorrelates before effectively climbing the potential well. In such noisy regime, the system behaves as a passive Brownian particle [18]. Finally, the self-alignment dynamics has a characteristic time of its own, given by  $\tau = (\beta v_0)^{-1}$ . Its role in the dynamical properties of the system will be discussed in detail in the coming sections.

In what follows, we express all quantities in dimensionless form using the following unit system:  $v_0/\mu$  for force,  $L_0$  for length, and  $\tau_0 = L_0/v_0$  for time. Numerical integrations of Eqs. (1) and (2) were performed following a fourth-order Runge-Kutta integrator, for the  $D = 0$  case, and a second-order stochastic Runge-Kutta integrator, for  $D > 0$ .

## III. DYNAMICAL STABILITY OF THE CLIMBING PHASE

For  $D = 0$ , the climbing phase corresponds to a static solution of Eqs. (1) and (2), given by  $\nabla V(x, y) = \hat{\mathbf{n}}$ , or

$$V_x(x_f, y_f) = \cos \theta_f, \quad V_y(x_f, y_f) = \sin \theta_f, \quad (3)$$

where  $V_x$  and  $V_y$  are the first derivatives of  $V$  with respect to  $x$  and  $y$ , respectively. This defines at least one curve in phase space where the absolute value of the confining force is constant and equals unity. We shall refer to such a curve as the *critical isoforce line* (CIL). In this work we shall assume that (i) the projection of the CIL onto the  $xy$  plane is a closed curve and (ii)  $V(x, y)$  is locally convex in the neighborhood of the CIL. These assumptions guarantee that the particle remains confined to the region enclosed by the CIL. Accordingly, we shall refer to potentials satisfying conditions (i) and (ii) as *confining potentials*.

Although the above conditions guarantee that the noise-free dynamics is bounded, in general they do not warrant stability of the climbing phase. From a dynamical systems perspective, each possible solution given by Eq. (3) is a fixed point of the system given by Eqs. (1) and (2) with  $D = 0$ . By performing linear stability analysis of the fixed points for an arbitrary confining potential  $V(x, y)$ , we have found that the stability of the climbing phase depends strongly on the self-alignment time  $\tau = \beta^{-1}$  (see Appendix A for details). In the absence of self-alignment ( $\beta = 0$ ), the climbing phase is always stable if the external potential satisfy conditions (i) and (ii) above. This finding generalizes a result previously obtained for an ABP confined in an isotropic harmonic potential [18,34], extending it to any confining potential  $V(x, y)$  with the properties described by conditions (i) and (ii).

When the self-alignment dynamics is considered ( $\beta > 0$ ), a point at the critical isoforce line becomes unstable when (see

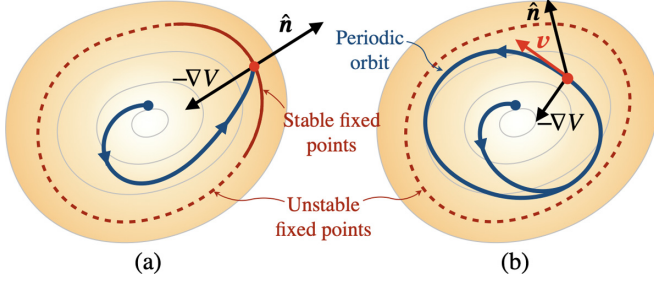


FIG. 1. Typical trajectories (blue lines) of an active particle (red dot) in a generic confining potential  $V(x, y)$  (contour plot) under two different situations: (a) For  $\beta < \beta^*$  (see text), the trajectory is attracted toward one of the available stable fixed points at the critical isoforce (red line). (b) For  $\beta > \beta^*$ , all fixed points are unstable and the particle is captured by one of the available orbital attractors.

#### Appendix A)

$$\beta > \min(\beta_1, \beta_2), \quad (4)$$

where

$$\beta_1 = V_{xx} + V_{yy},$$

$$\beta_2 = \frac{V_{xx}V_{yy} - V_{xy}^2}{V_x^2V_{xx} + V_y^2V_{yy} + 2V_xV_yV_{xy}}, \quad (5)$$

and  $V_\kappa$  and  $V_{\kappa\lambda}$  are, respectively, first and second derivatives of  $V(x, y)$  evaluated at the fixed point. As a first simple example, we consider a radially symmetric potential  $V(r)$ . As it follows trivially from Eq. (3), the critical isoforce line for any  $V(r)$  is a circle in the  $xy$  plane. By taking the radius of this circle as the unit of length ( $L_0$ ) and substituting in Eq. (5), we get  $\beta_1 = 1 + V_{rr}$  and  $\beta_2 = 1$  for all fixed points. Since  $V_{rr} > 0$ , all fixed points become unstable at simultaneously at  $\beta > 1$  for any  $V(r)$ . For potentials lacking radial symmetry, the typical situation is closer to that depicted in Fig. 1, where parts of the critical isoforce line become unstable before other ones. In this case, it is necessary to find the fixed points that maximize  $\beta_1$  and  $\beta_2$ . The critical isoforce becomes fully unstable when the last fixed points become unstable, that is,

$$\beta > \beta^* = \min[\max(\beta_1), \max(\beta_2)]. \quad (6)$$

To illustrate this, we analyze the anisotropic (elliptic) harmonic potential, expressed in dimensionless form by

$$V(x, y) = \frac{1}{2}[(1 + \varepsilon)x^2 + y^2], \quad (7)$$

where  $\varepsilon > 0$  is a parameter controlling the eccentricity of the potential. The critical isoforce in this case is an ellipse in the  $xy$  plane  $[(1 + \varepsilon)^2x^2 + y^2 = 1]$ . Evaluation of Eq. (4) gives  $\beta_1 = 2 + \varepsilon$  and  $\beta_2 = (1 + \varepsilon)/(1 + \varepsilon - \varepsilon y_f^2)$ . Notice that  $\beta_2 < \beta_1$  for all fixed points. The co-vertices of the ellipse,  $(x_f, y_f) = (\pm 1/(1 + \varepsilon), 0)$  are the first ones to become unstable, at  $\beta = 1$ . As  $\beta$  increases further, more points become unstable up to the last ones, at the vertices  $(x_f, y_f) = (0, \pm 1)$ , for  $\beta = \beta^* = 1 + \varepsilon$ . For  $\beta > \beta^*$ , there are no stable fixed points left for the system.

For any confining potential, on fulfillment of condition (6), the active particle has no option but to wander in perpetual orbital motion within the confining potential. Because of the highly nonlinear nature of the equations of motion, the

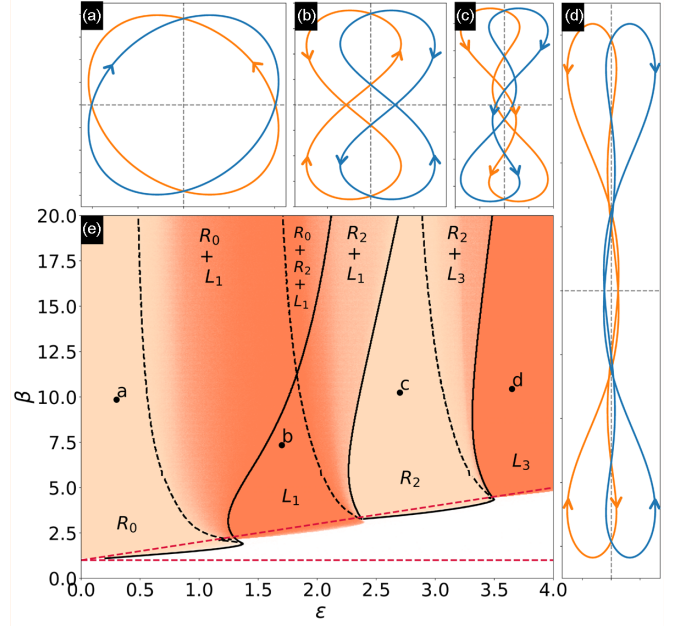


FIG. 2. [(a)–(d)] Representative orbits of an active particle in the elliptic potential. (e) Phase diagram in the plane defined by the self-alignment coefficient  $\beta$  and the potential eccentricity  $\varepsilon$ . The color shades indicate the topological state of the orbit obtained from random initial conditions (see text), light peach for rotation (R) and coral for libration (L). Full (dashed) lines indicate transitions between orbits when sweeping  $\varepsilon$  up (down) at fixed  $\beta$  values. The phases are classified by labels  $Xp$  according to their topology ( $X = R, L$ ) and number of nodes ( $p = 0, 1, 2, \dots$ ). Coexisting zones are marked with multiple labels. The straight dashed lines indicate the upper limit of the climbing phase ( $\beta = 1 + \varepsilon$ ) and the lower limit of the orbiting phases ( $\beta = 1$ , see Appendix D).

moving phase can only be determined accurately numerically, although some simple symmetry properties of periodic orbits can be inferred directly from the equations of motion (see Appendix C). In the coming sections, we discuss in detail the properties of periodic and chaotic orbits of confined active particles.

## IV. DETERMINISTIC ORBITAL PHASES

### A. Elliptical harmonic potentials

In contrast to the radially symmetric potentials, where only circular orbits are possible, the anisotropic potentials, such as the elliptic harmonic well, offer a range of rather involved closed orbits, featuring crossing points in the  $xy$  plane and specific topological properties. Some representative examples of observed orbits, obtained by numerical integration of Eqs. (1) and (2) with the potential given by Eq. (7), are illustrated in Figs. 2(a)–2(d). Notice that each orbital state is characterized by two orbits that are the exact mirror reflection of each other and rotate in opposite directions, which follows from the symmetry properties of the equations of motion and the confining potential (see Appendix C). By changing the eccentricity of the elliptic potential at fixed values of  $\beta$  we observed a sequence of transitions between orbital states of different shapes. These shapes always present at least one

of the symmetries discussed in Appendix C. They can be classified according to the number  $p$  of crossings performed by the projection of the particle trajectory into the  $xy$  plane:  $p = 0$  for oval orbits, as in Fig. 2(a);  $p = 1$  for lemniscates, as in Fig. 2(b); and  $p > 1$  for higher order generalized lemniscates, as in Figs. 2(c) and 2(d). Notice that the particle orientation  $\theta$  at a crossing point is different for each of the crossing branches, as required by the uniqueness theorem. The transitions between orbits typically satisfy:  $p \rightarrow p + 1$  for increasing  $\varepsilon$  and  $p \rightarrow p - 1$  for decreasing  $\varepsilon$ . In addition, to each of these orbits can be associated a topological charge, defined as

$$Q = \frac{1}{2\pi} \int_t^{t+T} d\theta, \quad (8)$$

where integration is taken along one period  $T$  of the orbit. From Eq. (1), a closed orbit in the  $xy$  plane implies  $\hat{\mathbf{n}}(t + T) = \hat{\mathbf{n}}(t)$  and thereby  $\theta(t + T) = \theta(t) + 2\pi \times \text{integer}$ . Therefore  $Q$  is an integer quantity. Below, we shall use  $Q$  to classify the orbits according to whether the orientation vector  $\hat{\mathbf{n}}$  of the particle performs full rotations ( $|Q| > 0$ ) or not ( $Q = 0$ ). For the case of the elliptic potential considered here,  $Q = \pm 1$  for all orbits with even  $p$ , meaning that  $\hat{\mathbf{n}}$  performs a full  $2\pi$  rotation within one period, either clockwise or counterclockwise. In contrast, orbits with odd  $p$  have  $Q = 0$ , meaning that  $\hat{\mathbf{n}}$  swings back and forth in librational motion, without ever performing a full rotation.

Another general observation is that the orbits tend to be more localized as  $\beta$  increases. In Appendix D, we derive the following analytical expression for the area within a closed loop described by the particle in the elliptic potential:

$$A_{\text{loop}} = \frac{\Delta\theta_{\text{loop}}}{(2 + \varepsilon)\beta}. \quad (9)$$

This exact formula reveals that the area of the lobes of any given orbit is a decreasing function of  $\beta$ , irrespective of the orbit shape. In particular, for full rotations, the total area of the orbit is  $A_{\text{orbit}} = 2\pi / [(2 + \varepsilon)\beta]$ .

A general view of the possible phases and phase transitions is presented in Fig. 2(e). The phases were classified according to the long-term steady-state dynamics, calculated numerically for each point of the  $\varepsilon\beta$  plane. We considered two different sets of initial conditions: (i) For a given  $\beta$  value, we initialize the system at the climbing (for  $\beta < 1$ ) or orbiting phase (for  $\beta > 1$ ) of the isotropic harmonic potential at  $\varepsilon = 0$  and slowly vary  $\varepsilon$  up to  $\varepsilon = 5$  and then back to 0, in steps of  $\Delta\beta = 0.16$  and  $\Delta\varepsilon = \pm 0.005$ . Transitions in the upward (downward) branch are depicted in the diagram as solid (dashed) lines. (ii) For each  $(\varepsilon, \beta)$  we initialize the system at 100 different random configurations and, for each of them, classify the orbit as either rotation (light peach) or libration (coral), in steps of  $\Delta\beta = 0.038$  and  $\Delta\varepsilon = 0.01$ . The color gradients indicate the percentage of each phase in the sample of 100 initial conditions.

A salient feature in the phase diagram presented in Fig. 2 is that some orbits can coexist in the same region of the parameter space. For  $D = 0$ , the actual orbit performed by the particle depends on the initial conditions and on the specific history of the control parameters. Indeed, all observed orbital transitions are characterized by hysteretic behavior when sweeping  $\varepsilon$  up

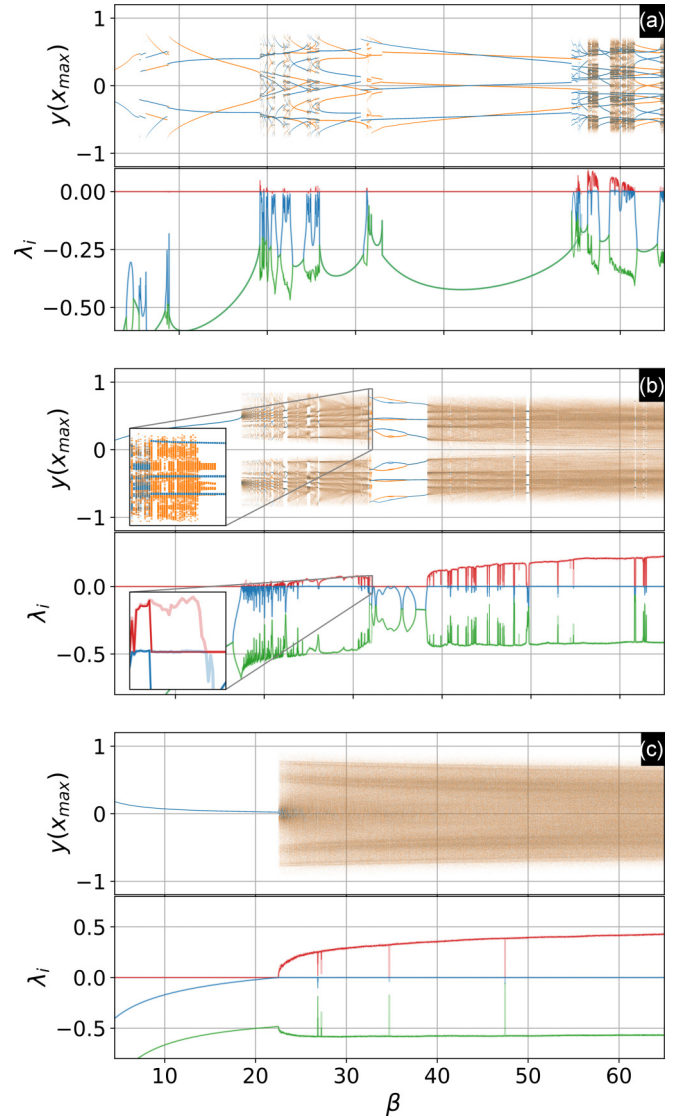


FIG. 3. (a) Bifurcation diagram (top) and Lyapunov spectrum (bottom) for the anharmonic potential  $V(x, y) = \frac{1}{2}(x^2 + y^6)$ . The diagram is generated by plotting the  $y$  position of the particle every time  $x$  reaches a maximum value for increasing (orange) and decreasing (blue)  $\beta$ . The Lyapunov exponents corresponding to increasing (decreasing)  $\beta$  are depicted in light (corresponding dark) colors. Red, blue, and green correspond, respectively, to the largest, the second largest, and the smallest exponent. [(b) and (c)] Same as (a) but for the potentials  $V(x, y) = \frac{1}{6}(2x^2 + y^2)^3$  and  $V(x, y) = \frac{1}{6}(x^6 + y^6)$ , respectively.

and down. The hysteresis is more pronounced for larger values of  $\beta$ . For example, in Fig. 2 we observe that the transitions  $p \rightarrow p + 1$  occur at decreasing  $\beta$  as  $\varepsilon$  increases. However, for decreasing  $\varepsilon$  the  $p \rightarrow p - 1$  transitions have a quite different dependence on  $\varepsilon$ . The coexisting regions of different orbits are delimited by these transition lines. In addition, there also can be coexistence between orbital and climbing phases (small regions depicted below the  $\beta = 1 + \varepsilon$  line). It is proven in Appendix D that orbital motion is prohibited for  $\beta < 1$  for any  $\varepsilon$ .

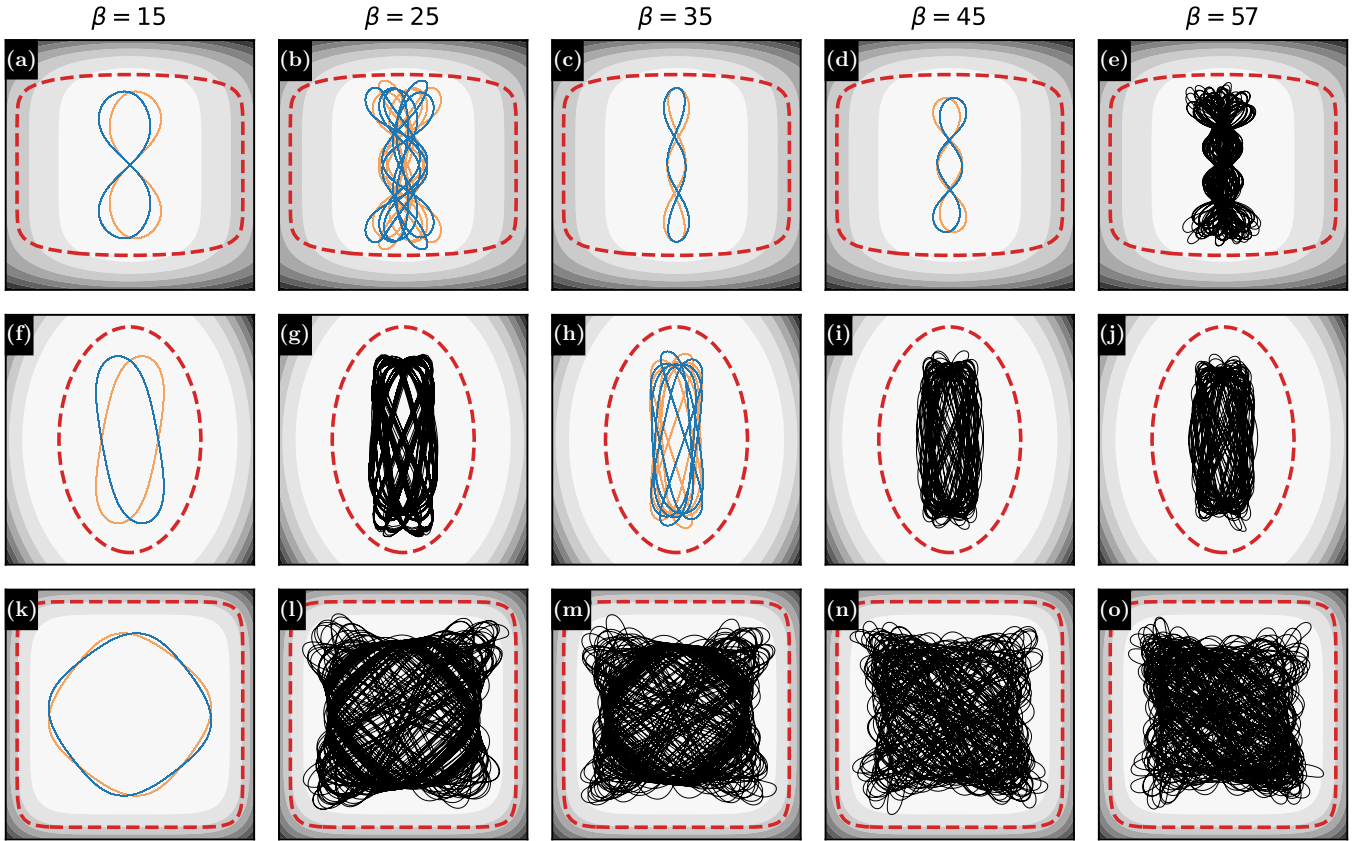


FIG. 4. Examples of periodic (blue and orange lines) and chaotic (black lines) orbits for an active particle confined to the anharmonic potentials: [(a)–(e)]  $V(x, y) = \frac{1}{2}(x^2 + y^6)$ , [(f)–(j)]  $V(x, y) = \frac{1}{6}(2x^2 + y^2)^3$ , and [(k)–(o)]  $V(x, y) = \frac{1}{6}(x^6 + y^6)$ . The background color gradients represent the potential, with lighter shades indicating lower energy values. The dashed lines depict the critical isoforce line (CIL), which is fully unstable for all  $\beta$  values considered (labels at the top). For the periodic orbits, (a)–(d), (f), (h), and (k), we show both trajectories allowed by symmetry.

**B. Anharmonic potentials and chaos**

We have shown above that an active particle confined in radially symmetric potentials, either harmonic or anharmonic, can only perform circular orbits and that breaking the radial symmetry of a harmonic potential induces different kinds of noncircular orbits with different topological properties. Here we explore confining potentials which are both asymmetric and anharmonic and show that this combination can lead the active particle to perform chaotic orbits for sufficiently large values of the self-alignment coefficient  $\beta$ .

To illustrate this, we consider three anisotropic and highly nonlinear potentials, (i)  $V(x, y) = \frac{1}{2}(x^2 + y^6)$ , (ii)  $V(x, y) = \frac{1}{6}(2x^2 + y^2)^3$ , and (iii)  $V(x, y) = \frac{1}{6}(x^6 + y^6)$ , and analyze the long-term dynamics as a function of  $\beta$ . In all three cases, we start the particle in the climbing phase at  $\beta < 1$  and slowly sweep  $\beta$  up to  $\beta = 80$  and then down to  $\beta = 1$  in steps of 0.01. For each new  $\beta$  value, the swimmer is initialized at the last state calculated in the previous step and the dynamical state is analyzed after a waiting time  $\Delta t_{\text{wait}} = 5 \times 10^3 \tau_0$  over a measuring time window  $\Delta t_{\text{meas}} = 10^4 \tau_0$ .

Figure 3 shows bifurcation diagrams and Lyapunov spectra for an active particle confined to each of the considered anharmonic potentials. The bifurcation diagrams were obtained by recording for each  $\beta$  the  $y$  position of the active particle every time  $x$  reaches a maximum ( $x_{\text{max}}$ ) during the measuring

time (which typically covers about 500 cycles of  $x$ ). For some ranges of  $\beta$  values, specially for small  $\beta$ , all measures of  $y(x_{\text{max}})$  collapse to a small set of points, thus indicating the system is under periodic motion. A few examples of periodic orbits are shown in Figs. 4(a)–4(d), 4(f), 4(h), and 4(k). Notice that some of them are rather involved, though perfectly periodic, and all of them have a twin sister orbit rotating in the opposite direction. However, for other ranges of  $\beta$  values, the points  $y(x_{\text{max}})$  are largely dispersed, which is indicative of aperiodic motion, like those exemplified in Figs. 4(e), 4(g), 4(i), 4(j), and 4(l)–4(o).

To check if the aperiodic phases are indeed chaotic, we calculated numerically the Lyapunov spectrum for each value of  $\beta$  following the tangent map method [35]. For any confining potential, the orbital phase corresponds to bounded trajectories in the three-dimensional phase space spanned by the variables  $x$ ,  $y$ , and  $\theta$ . The response of the system to small perturbations of these trajectories are thereby described by three Lyapunov exponents. One of them is always zero, thus reflecting perturbations along the otherwise undisturbed trajectory. The other two exponents can be used to determine whether the dynamics is regular (all exponents are nonpositive) or chaotic (at least one exponent is positive). In the latter case, the positive exponent reflects the exponential sensitivity to initial conditions. Notice that all aperiodic regions of the

bifurcation diagrams have a positive Lyapunov exponent and thereby are chaotic.

Overall, notwithstanding windows of periodic behavior, the sensitivity to initial conditions revealed by the positive Lyapunov exponent tends to increase with  $\beta$  for all three numerical experiments of Fig. 3. That is, a swimmer trapped by a highly nonlinear potential tends to exhibit more chaotic behavior if it has a stronger self-alignment torque. As for the effect of the nonlinearity of the confining potential, we have also evaluated other potentials of the type  $V(x, y) = \frac{1}{2\alpha}(2x^2 + y^2)^\alpha$ , for  $\alpha = 1.5$  to 5 in steps of 0.5. Within the range  $1.0 < \beta < 80$ , chaotic behavior was only observed for  $\alpha = 2.5$  and 3. For all other  $\alpha$  values only periodic orbits were observed. We believe the absence of chaos for high values of the exponent  $\alpha$  might be related to the fact that in this case the confining potential becomes too flat in the middle, so that the particle can only change direction when it is close to the CIL. For this reason, the active particle follows closely the CIL, leaving little room for more complex orbits. But this is not to be taken as a general rule. For instance, inertial effects, not considered in this work, might cause the particle to bounce off the CIL [27], allowing it to make more involved excursions throughout the potential well.

Finally, looking closely at the bifurcation diagrams of Fig. 3, one can identify hysteresis in some intervals of  $\beta$  values. In most of these intervals, different periodic orbits coexist, similarly to what was observed for the elliptic harmonic potential. In more rare occasions, coexistence between a periodic orbit and a chaotic attractor can be identified in very narrow windows of  $\beta$  values [see insets in Fig. 3(b)].

## V. DYNAMICAL PHASES AT FINITE NOISE

Next we turn our attention to some phenomena related to finite noise intensities ( $D > 0$ ). The main quantity we used to identify the effect of noise is the probability distribution functions (PDF)  $\mathcal{P}(x, y)$  and  $\mathcal{P}(\theta)$ . For a given confining potential and noise intensity  $D$  the PDFs were calculated by averaging the steady-state dynamics of  $10^4$  particles, over a measuring time  $5 \times 10^3 \tau_0$ , and after a waiting time of  $10^3 \tau_0$ , unless stated otherwise.

### A. Noise-induced crossover from active to passive behavior

For conventional active particles trapped in an isotropic potential, the PDF under small noise intensities  $D$  is known to be highly localized radially at a finite distance from the center of the potential. In contrast, the angular motion of the particle is diffusive, resulting in a ring-shaped PDF in the  $xy$  plane. As one increases  $D$ , the ring shrinks while the PDF becomes less and less localized until, for large-enough  $D$  (typically  $D \gg v_0/L_0$ ), the PDF collapses into a Boltzmann-like distribution with a peak at the trap minimum [17,18]:

$$\mathcal{P}(x, y) \propto \exp[-\mu V(x, y)/D_{\text{eff}}], \quad (10)$$

where  $D_{\text{eff}} = v_0^2/2D$  is the effective diffusion constant [29].

To check whether this scenario also applies to anisotropic potentials, we calculated numerically the probability distribution function of the active particle trapped by an elliptic harmonic potential of eccentricity  $\varepsilon = 1$  for different values

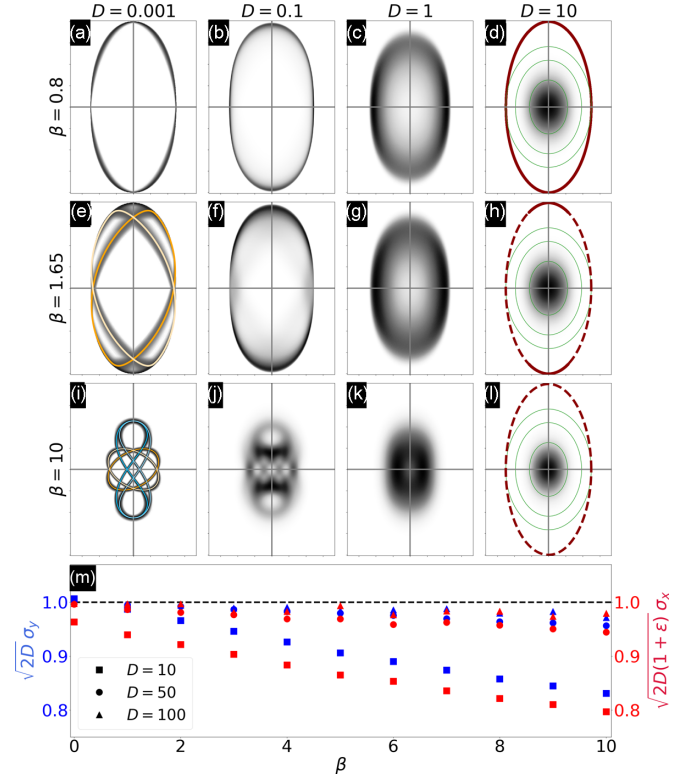


FIG. 5. [(a)–(l)] Density plots of the steady-state probability distribution function  $\mathcal{P}(x, y)$  of an active particle in the elliptic harmonic potential with  $\varepsilon = 1.0$  for different values of the self-alignment coefficient  $\beta$  and noise intensity  $D$ . The grayscale in the first column [(a), (e), and (i)] was set to logarithmic for better visualization. In (d), (h), and (l), the solid (dashed) red lines depict the stable (unstable) segments of the critical isoforce, while the green lines are equipotentials of  $V(x, y)$ . Light solid lines in (e) and (i) depict the possible noise-free orbits. (m) Scaled standard deviates of the particle coordinates as a function of  $\beta$ . The dashed line is the  $\beta = 0$  theoretical limit,  $\sqrt{2D}\sigma_y = \sqrt{2D(1 + \varepsilon)}\sigma_x = 1$ , obtained from Eq. (10).

of  $D$  and  $\beta$ . We start our analysis considering the climbing phase ( $\beta < 1$ ), where the realignment dynamics is expected to play little role and the system behaves as a conventional ABP. In Figs. 5(a)–5(d), we present the PDFs for  $\beta = 0.8$  and a few representative values of  $D$ . This value of  $\beta$  falls in the region of the phase diagram where the critical isoforce is fully stable. In this case, the evolution of the PDF with  $D$  follows approximately the typical behavior of a conventional ABP described above. However, in contrast to the isotropic case, here the aspect ratio of the PDF changes with  $D$ . For small  $D$ , the aspect ratio coincides with that of the critical isoforce line, given by  $1 + \varepsilon = 2$ , since in this case the thermal time  $\tau_{\text{th}} = 1/D$  is large compared with the other characteristic timescales and, thereby, the PDF is dominated by the force balance condition Eq. (3). For large  $D$ , the aspect ratio coincides with that of the equipotential lines:  $\sqrt{1 + \varepsilon} = \sqrt{2}$ . This reveals the dominance of diffusion in the high  $D$  limit, in which case the PDF follows the contours of the potential well, as follows from Eq. (10). Therefore, this geometrical crossover conveniently reflects the different mechanisms behind the PDF of an active particle at different noise levels.

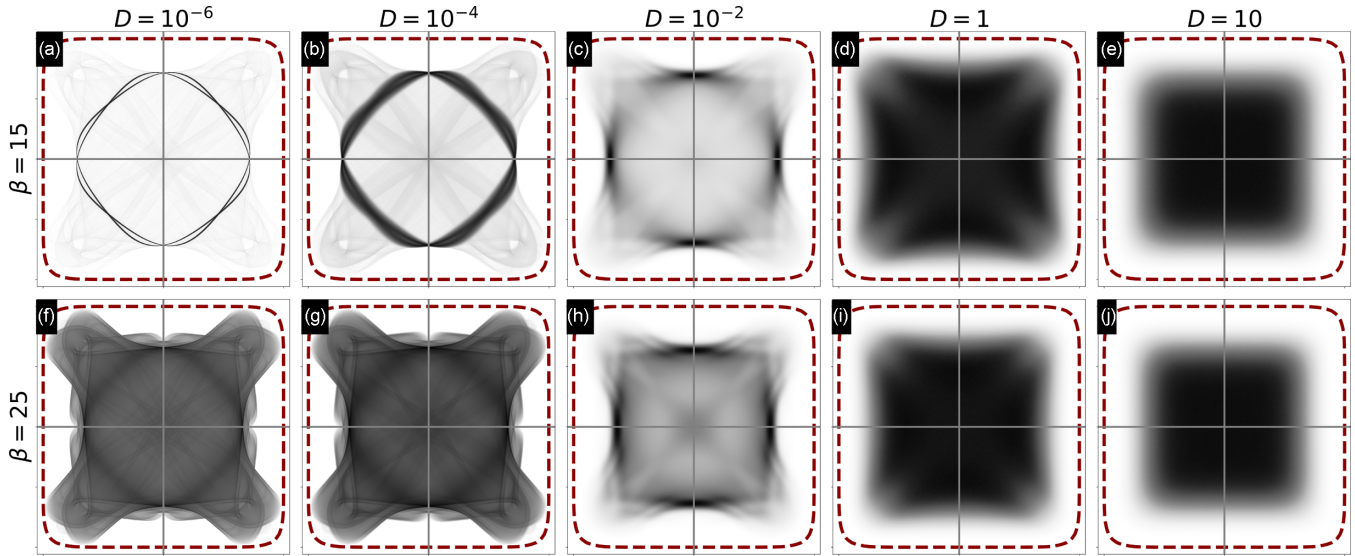


FIG. 6. Density plots of the steady-state probability distribution function  $\mathcal{P}(x, y)$  of an active particle in the anharmonic potential  $V(x, y) = \frac{1}{6}(x^6 + y^6)$  for different noise intensities  $D$  and  $\beta = 15$  (top) and  $25$  (bottom). The grayscale in the first two columns [(a), (b), (f), and (g)] was set to logarithmic for better visualization. Red dashes depict the unstable critical isoforce line.

For moderate values of  $\beta$  ( $1 < \beta < 1 + \varepsilon$ ) the critical isoforce is no longer fully stable and orbits can coexist with the climbing phase. This changes dramatically the PDF at low noise, as seen in Fig. 5(e), where the particles are highly localized around the deterministic R0 orbits and the stable part of the critical isoforce. For larger  $D$ , however, the climbing phase seems to dominate the PDF until the Boltzmann-like behavior is achieved at  $D \sim 10$  [see Figs. 5(f) and 5(g)].

For large  $\beta$ , the self-alignment dynamics plays a dominant role in the deterministic limit, inducing the wealth of orbital phases discussed in the previous section. The effect of noise in the high- $\beta$  regime is illustrated in Figs. 5(i)–5(l). For both low ( $D \ll 1$ ) and moderate ( $D \lesssim 1$ ) noise the PDF follows closely the deterministic orbits, thus revealing the resilience of the orbits and thereby of the self-alignment dynamics in these noise regimes. Once again, for  $D \gg 1$ , the distribution follows the Boltzmann-like behavior. However, the effect of the self-alignment torque is still noticed at such high noise intensities. The PDF in this case becomes more localized for larger values of  $\beta$ , which we believe is reminiscent of the  $1/\beta$  dependence of the area enclosed by loops [see Eq. (9)]. This is evidenced in Fig. 5(m), where the standard deviation of the particle coordinates is shown to decrease with  $\beta$ . Therefore, the effective diffusion constant of an active particle with self-alignment torque is a function not only of  $D$  and  $v_0$ , like in the conventional ABP model, but also of the self-alignment coefficient  $\beta$ .

### B. Noise-induced complex orbits

For  $\beta \lesssim 1$ , the noise-driven dynamics of the active particle in an anisotropic anharmonic potential follows a scenario similar to its harmonic counterpart. However, for large  $\beta$ , the anharmonic potentials still reserve some surprises. In Fig. 6 we present PDFs of the active particle trapped in the potential  $V(x, y) = \frac{1}{6}(x^6 + y^6)$  as a function of noise for two different self-alignment torque intensities,  $\beta = 15$  and  $25$ . As shown in Figs. 4(k) and 4(l) [see also Fig. 3(c)], the deterministic

dynamics is periodic for  $\beta = 15$  and chaotic for  $\beta = 25$ . Surprisingly, when noise is turned on, the PDFs for  $\beta = 15$  reveal that the periodic orbit actually coexists with a complex set of visited points, which resembles the chaotic attractor observed for  $\beta = 25$ . Notice that for small  $D$  values, the probability of finding the particle in the complex set is several orders of magnitude smaller than that of finding it in the periodic orbit in the  $\beta = 15$  case. For this reason, we use a logarithmic gray scale for the low-noise PDFs. Still, the rare excursions of the particle outside its periodic orbits follow a beautiful complex pattern. This is in stark contrast with the periodic orbits observed for the harmonic potentials shown in Fig. 5, where noise at low  $D$  induces only a slight spreading of the PDF around the deterministic orbits. For  $D \gtrsim 10^{-2}$ , the similarity between the PDF for  $\beta = 15$  and  $\beta = 25$  can already be appreciated in linear scale, as the periodic orbits seem to be washed out within this noise range. For strong noise ( $D \gtrsim 1$ ), the PDF in both cases assumes the shape of a cross pattée [Figs. 5(d) and 5(i)] before finally collapsing to a Boltzmann-like distribution at  $D \sim 10$  [Figs. 5(e) and 5(j)]. Although the pattern revealed by the PDFs for both  $\beta$  values are qualitatively similar, there is an important difference as concerns their physical origin. The chaotic set for  $\beta = 25$  is an attractor in the deterministic limit and dominates the dynamics also for low and moderate noise intensities. By solving the deterministic ( $D = 0$ ) dynamics of the particle starting from  $10^5$  randomly chosen initial conditions, we have verified that for  $\beta = 15$  the periodic orbit is the only deterministic attractor, while the chaotic set is a nonattractive, transient chaotic set with a lifetime of the order  $10^3 \tau_0$  (see Fig. 7). This means that, in the deterministic limit, the chaotic set, shown in the inset of Fig. 7, dominates the dynamics only during finite timescales, as the system evolves from a given initial condition toward the true long-term state: the periodic orbit. However, for sufficiently large noise, this nonattractive chaotic set re-emerges and begins to dominate the long-term dynamics, as more and more often the particle leaves its periodic orbit to explore

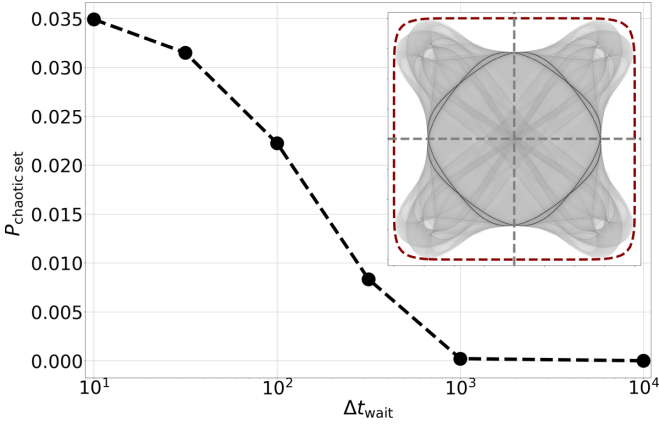


FIG. 7. Probability of finding the particle in the transient chaotic set, calculated after a waiting time  $\Delta t_{\text{wait}}$ , as a function of  $\Delta t_{\text{wait}}$  for  $D = 0$  and  $\beta = 15$ . Inset: Probability density function for  $\Delta t_{\text{wait}} = 10\tau_0$ , featuring the transient chaotic set and the periodic orbits.

the chaotic set. This phenomenon is known as noise-induced chaos [36] and has been relevant for the phenomenology of, e.g., driven Josephson junctions [37], neuronal models [38], and population dynamics [39].

### C. Coexisting orbital phases

The large coexistence regions between different periodic orbits seen in the phase diagram of the elliptical harmonic trap

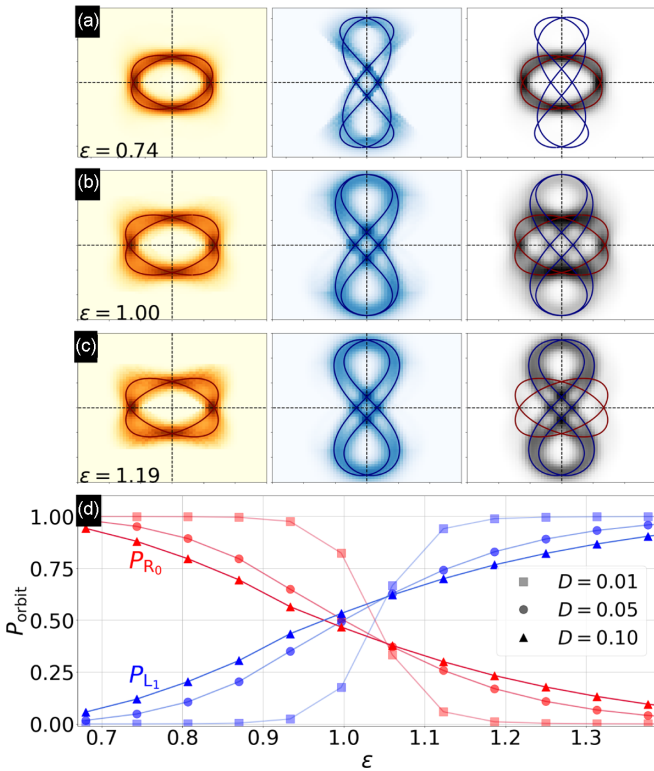


FIG. 8. [(a)–(c)] Density plots of the stationary probability distribution functions of finding the particle in phase R0 (left), L1 (middle), and anywhere (right) for different eccentricities  $\varepsilon$  and fixed  $\beta = 10$  and  $D = 0.05$ . (d) Total probabilities of finding the particle either in the R0 (red) and L1 (blue) phases as a function of  $\varepsilon$  for different noise intensities and fixed  $\beta = 10$ .

(Fig. 2) allows for an in-depth investigation on how the probability of finding the particle in a particular orbit changes as a function of a control parameter. To perform this study, we fix  $\beta = 10$  and sweep  $\varepsilon$  in the range  $0.8 < \varepsilon < 1.3$ , thus covering approximately a full width of the coexistence zone between the oval (R0) and the lemniscate (L1) orbits. To determine whether a particular configuration of the swimmer belongs to one orbit or to the other, we previously compute the basins of attraction of the R0 and L1 orbits in phase space [40]. This allows us to calculate the PDF of finding the swimmer in a particular orbit. These partial PDFs along with the joint PDF are plotted in Figs. 8(a)–8(c) for  $D = 0.05$  and a few different values of the potential eccentricity. The integrated probabilities of finding the particle in the R0 phase,  $P_{R0}$ , or in the L1 phase,  $P_{L1}$ , are shown in Fig. 8(d) for three different noise intensities. These results reveal that, as  $\varepsilon$  increases, the PDF continuously crosses over from a distribution dominated by the R0 orbits to that typical of a L1 orbit, resembling the typical behavior of a thermodynamic two-level system, with the eccentricity  $\varepsilon$  playing the role of the energy-level separation and  $D$  playing the role of temperature.

## VI. CONCLUSIONS

In summary, we have investigated the dynamics of an active Brownian particle with self-alignment torque in the presence of diverse confining potentials. We derived analytical expressions for the stability condition of the climbing phase for an arbitrary confining potential, which allowed us to conclude that this static phase always gives place to orbital motion at a sufficiently strong self-alignment torque. Then, we set out to investigate numerically possible orbital phases as a function of self-alignment torque and confining potential shape.

For the case of elliptical harmonic potentials, we have shown that breaking the rotational symmetry leads to a complex dynamical phase diagram featuring periodic orbits with different topological properties that can be assessed by tuning the potential eccentricity and the self-alignment torque coefficient  $\beta$ . Under moderate noise, coexisting orbits follow statistics similar to equilibrium two-state systems, while for strong noise both orbital and climbing phases collapse to a Boltzmann-like distribution, revealing a passive-Brownian-particle type of behavior with an effective diffusion constant that depends on the propulsion speed  $v_0$  and on  $\beta$ .

For anharmonic potentials, we reported transitions from periodic orbital motion to chaos as one increases the intensity of the self-alignment torque. Our results suggest that chaotic motion of the confined active particle can be observed for short self-alignment time and a suitable degree of nonlinearity of nonradially symmetric confining potentials. Interestingly, even for  $\beta$  values where periodic orbits are the only possible long-term state, transient chaotic sets can be activated and dominate the long-term system dynamics at small but strong-enough noise. Recently, transient chaos has been investigated in the context of interacting active particles in a trap [41,42]. Here we showed that it can play a significant role to the orbital motion of trapped active particles already in the single particle level.

These results reveal that a single active particle trapped in anisotropic potentials can exhibit surprisingly rich phenomena



that could be relevant for real-life active matter, such as living systems, and robotic metamaterials. They also open up new venues of research that go beyond the scope of the present work. For example, the coexisting orbital phases revealed here raises the question of whether the noise-induced escape rate from one orbit into another follows some kind of Kramers law, in a way similar to the escape problem of an active particle from a trap [20–22]. Another direction is the study of the effect of inertia, which has recently been shown to induce orbits in circular confinement even without self-alignment torque [27]. The anisotropic confinement could be used to distinguish between the contribution of both effects. Finally, the chaotic orbits shown here could be used to explore, e.g., synchronization phenomena induced by the interaction between two or more active particles [43].

### ACKNOWLEDGMENTS

We thank M. Copelli, A. Rosas, and D. Canavello for useful suggestions. This work was supported by the Brazilian Agencies CNPq (Conselho Nacional de Desenvolvimento Científico e Tecnológico) and CAPES (Coordenação de Aperfeiçoamento de Pessoal de Nível Superior) through the program PROEX (Programa de Excelência Acadêmica) Grant No. 23038.003069/2022-87.

### APPENDIX A: STABILITY ANALYSIS OF THE CLIMBING PHASE

In dimensionless form, the noise-free version of Eqs. (1) and (2) can be expressed as

$$\begin{aligned}\dot{x} &= \cos \theta - V_x(x, y) \\ \dot{y} &= \sin \theta - V_y(x, y) \\ \dot{\theta} &= \beta[V_x(x, y) \sin \theta - V_y(x, y) \cos \theta].\end{aligned}\quad (\text{A1})$$

It is also convenient to express this system in vector form,  $\dot{\mathbf{R}} = \mathbf{A}(\mathbf{R})$ , where  $\mathbf{R} = (x, y, \theta)$  and  $\mathbf{A}$  is a vector field whose components are given by the right-hand side of Eq. (A1). The fixed points of this autonomous dynamical system are obtained by taking  $\dot{x} = 0$ ,  $\dot{y} = 0$ , and  $\dot{\theta} = 0$ , leading to Eq. (3). Their stability can be evaluated straightforwardly by evaluating the linearized version of Eq. (A1):  $\delta \dot{\mathbf{R}} = \mathbf{J} \delta \mathbf{R}$ , where  $\mathbf{J}$  is the Jacobian matrix of  $\mathbf{A}$  and  $\delta \mathbf{R} = \mathbf{R} - \mathbf{R}_f$  are small displacements from the considered fixed point  $\mathbf{R}_f$ . For an arbitrary potential  $V(x, y)$ , the eigenvalues of the problem are

$$\lambda_0 = 0, \quad \lambda_{\pm} = \frac{p_1 \pm \sqrt{p_1^2 + 4p_0}}{2}, \quad (\text{A2})$$

where  $p_0 = \beta(V_x^2 V_{xx} + V_y^2 V_{yy} + 2V_x V_y V_{xy}) - V_{xx} V_{yy} + V_{xy}^2$  and  $p_1 = \beta - V_{xx} - V_{yy}$ . The eigenvector associated to the null eigenvalue corresponds to displacements along the line of fixed points in the three-dimensional phase space. The other two eigenvalues can be either positive or negative, depending on the value of  $\beta$ , and are associated to directions orthogonal to the line of fixed points. We say a fixed point is stable if the real part of both these eigenvalues is negative. One has to keep in mind, however, that such stability is related only to fluctuations that drive the system away from the line of fixed

points. Fluctuations along the fixed point line can make the system wander from fixed point to fixed point.

For  $\beta = 0$ , one has  $p_0 = -\Delta$  and  $p_1 = -\tau$ , where  $\Delta = V_{xx} V_{yy} - V_{xy}^2$  and  $\tau = V_{xx} + V_{yy}$  are, respectively, the determinant and the trace of the Hessian matrix of  $V(x, y)$  evaluated at the fixed points. Since  $V(x, y)$  is a confining potential, it must be convex at the critical isoforce, that is,  $V_{xx} > 0$ ,  $V_{yy} > 0$ , and  $\Delta > 0$ . In this case,  $p_0 < 0$  and  $p_1 < 0$ , which guarantees that  $\lambda_+$  and  $\lambda_-$  are both negative. Therefore, the fixed points are always stable in the absence of the self-alignment term ( $\beta = 0$ ).

In the general case ( $\beta \geq 0$ ),  $\lambda_+$  is positive for all  $p_1 > 0$  or, in case  $p_1 < 0$ , for all  $p_0 > 0$ . This leads to two upper limit values of  $\beta$  for the stability of the fixed point:

$$\begin{aligned}\beta_1 &= V_{xx} + V_{yy}, \\ \beta_2 &= \frac{V_{xx} V_{yy} - V_{xy}^2}{V_x^2 V_{xx} + V_y^2 V_{yy} + 2V_x V_y V_{xy}}.\end{aligned}\quad (\text{A3})$$

The fixed point becomes unstable if  $\beta > \min(\beta_1, \beta_2)$ . Notice that, due to the required local convexity of  $V(x, y)$  at the critical isoforce, both  $\beta_1$  and  $\beta_2$  are positive for all fixed points.

### APPENDIX B: RADially SYMMETRIC CONFINEMENT

#### 1. Climbing phase

For radially symmetric potentials,  $V(r)$ , it is convenient to rewrite Eq. (A1) in terms of the polar coordinates  $(r, \phi)$  of the particle position,

$$\begin{aligned}\dot{r} &= \cos \chi - V'(r) \\ \dot{\phi} &= r^{-1} \sin \chi \\ \dot{\theta} &= \beta V'(r) \sin \chi,\end{aligned}\quad (\text{B1})$$

where  $\chi = \angle(\hat{\mathbf{n}}, \mathbf{r}) = \theta - \phi$ . It then becomes clear that the fixed points satisfying  $(\dot{r}, \dot{\phi}, \dot{\theta}) = (0, 0, 0)$  are given by  $r_f = R$  and  $\theta_f = \phi_f$ . Therefore, for any shape of  $V(r)$ , the critical isoforce line is a circle of radius  $R$ . By taking  $R$  as the unit of length, Eq. (A3) gives

$$\beta_1 = 1 + V''(1) \quad \text{and} \quad \beta_2 = 1 \quad (\text{B2})$$

for all fixed points. Since  $V''(1) > 0$  as required by the convexity of  $V(r)$ , all fixed points become unstable when  $\beta > 1$ .

#### 2. Orbital phase

To find the possible orbits for circularly symmetric potentials, it is convenient to express Eq. (B1) in terms of  $r$ ,  $\phi$ , and  $\chi = \theta - \phi$ . This amounts to replacing the equation of the orientational dynamics by  $\dot{\chi} = [\beta V'(r) - \frac{1}{r}] \sin \chi$ . It then becomes transparent that the system admits a stationary solution ( $\dot{r} = 0$ ,  $\dot{\phi} = \omega$ ,  $\dot{\chi} = 0$ ) where the particle performs a circular orbit with constant radius  $R_o$ , angular velocity  $\omega$ , and tilt angle  $\chi_o$ , given respectively by

$$V'(R_o) = \frac{1}{\beta R_o}, \quad (\text{B3})$$

$$\omega = \frac{1}{R_o} \sqrt{1 - \frac{1}{\beta^2 R_o^2}}, \quad (\text{B4})$$

and

$$\chi_0 = \arccos[V'(R_0)]. \quad (\text{B5})$$

Since  $\dot{\chi} = 0$ , one has  $\dot{\theta} = \dot{\phi} = \omega$ , that is, both vectors,  $\mathbf{r}$  and  $\hat{\mathbf{n}}$ , rotate at constant speed, keeping a constant angle  $\chi_0$  between each other. Notice that Eq. (B4) requires that  $\beta R_0 > 1$ . Therefore, from (B3),  $V'(R_0) < 1$ , that is, the orbit necessarily lies in the subcritical region,  $R_0 < 1$ , and thereby  $\beta > 1$  turns out to be a necessary condition for circular orbits in radially symmetric potentials. In particular, this condition is satisfied for all power-law central force potentials  $V = r^n/n$  for all  $n > 1$ . The special case  $n = 2$  was investigated thoroughly in Ref. [26].

To check the stability of this solution, we evaluate Eq. (B1) in the vicinity of a circular orbit within linear approximation, using the same method described in Appendix A, but this time the relevant, independent variables are  $r$  and  $\chi$ . The eigenvalues associated to small displacements of the circular orbit are

$$\lambda_{\pm} = \frac{-V'' \pm \sqrt{V''^2 - 4\beta\omega^2 R_0^2 (V'' + V'/R_0)}}{2}, \quad (\text{B6})$$

where  $V''$  and  $V'$  are evaluated at the orbit radius. Notice that  $\text{Re}(\lambda_{\pm})$  and  $\text{Re}(\lambda_{\mp})$  are both negative as long as  $V''$  and  $V'$  are both positive. In this case, circular orbits are stable solutions (limit cycles) for all  $\beta > 1$ .

The stability of circular orbits is not restricted to monotonically increasing  $V(r)$ . To illustrate this, we consider the ‘‘Mexican hat’’ potential  $V(x, y) = \frac{1}{2}(r^4 - r^2)$ . This potential allows for stable circular orbits for all  $\beta$ , with maximum radius  $R_0 = 1$  and orientation  $\chi_0 = 0$ , for  $\beta \rightarrow 1^+$ , and minimum radius  $R_0 = 1/\sqrt{2}$  and orientation  $\chi_0 = \pi/2$ , for  $\beta \rightarrow \infty$ . In Fig. 9, we present the noise-averaged properties of the orbital motion of an active particle in the Mexican hat potential with  $D = 0.01$  as a function of  $\beta$ . The results are in excellent agreement with the theoretical noise-free result, indicating that the mean radius of the orbit,  $\langle R_0 \rangle$ , as well as the mean inclination of the particle orientation vector,  $\langle \chi_0 \rangle$ , are resilient to fluctuations for moderate noise.

### APPENDIX C: TOPOLOGICAL AND SYMMETRY PROPERTIES OF ORBITS

In this section we demonstrate two results concerning properties of orbits related to the confinement potential symmetry.

*Theorem C.1.* To any part of a given orbit in a confining potential with reflection symmetry there corresponds a reflected part in which the particle moves with the opposite handedness.

*Proof.* For a confinement potential with reflection symmetry, described by an improper orthogonal transformation,  $\mathbf{S}$ , vectors will be transformed as  $\mathbf{v}^{(S)} = \mathbf{S}\mathbf{v}$ , while pseudovectors as  $\mathbf{v}^{(S)} = (\det \mathbf{S})\mathbf{S}\mathbf{v}$ . Eq. (1) is vector equation, while (2) a pseudovector one, since we have a cross product.

For the sake of simplicity let us take the  $y$  axis as the line of reflection. Thus,  $\mathbf{S}$  is an improper rotation given by

$$\mathbf{S}_y = \begin{pmatrix} -1 & 0 \\ 0 & 1 \end{pmatrix} \quad (\text{C1})$$

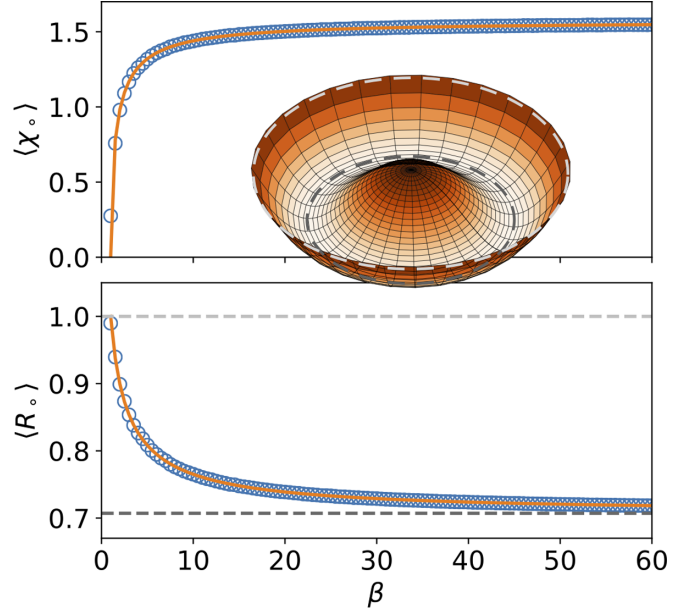


FIG. 9. Mean angle  $\chi_0$  between  $\hat{\mathbf{n}}$  and  $\mathbf{r}$  (top) and mean orbital radius (bottom) for an active particle confined in the potential  $V(r) = \frac{1}{2}(r^4 - r^2)$  with  $D = 0.01$  (symbols). Full lines represent the noise-free analytical results. Inset: Surface plot of  $V(r)$ . Light and dark dashes indicate respectively the maximum and the minimum values of the orbit radius.

for which  $\det \mathbf{S}_y = -1$ . In this case, Eq. (1) yields  $\dot{x}^{(S)} = -\dot{x}$ ,  $\dot{y}^{(S)} = \dot{y}$  (which means motion in a reversed direction on the  $xy$  plane), while Eq. (2) provides  $\dot{\theta}^{(S)} = -\dot{\theta}$ . Additionally, for  $\theta$  we have  $n_x^{(S)} = \cos \theta^{(S)} = -\cos \theta$ ,  $n_y^{(S)} = \sin \theta^{(S)} = \sin \theta$ . Together with  $\dot{\theta}^{(S)} = -\dot{\theta}$ , we obtain  $\theta^{(S)} = -\theta + (2m + 1)\pi$ ,  $m$  integer. Therefore, the reflection symmetry of the confinement potential leads to reflected points of a given orbit to be also solutions of Eqs. (1) and (2) with reversed motion, with  $\theta \rightarrow -\theta \pm \pi$  for reflection on the  $y$  axis. ■

*Theorem C.2.* For confinement potentials with  $N$ -fold rotational symmetry any given part of a particle trajectory has a corresponding multiple of  $2\pi/N$  rotated part in which the particle moves with the same handedness.

*Proof.* For a confinement potential having  $N$ -fold rotational symmetry, let us denote the proper orthogonal transformation as  $\mathbf{R}_N$ , where  $\det \mathbf{R}_N = 1$ . Therefore,  $\dot{\mathbf{r}}^{(R_N)} = \mathbf{R}_N \dot{\mathbf{r}}$  is the velocity vector rotated by  $2\pi/N$  and Eq. (2) provides  $\dot{\theta}^{(R_N)} = \dot{\theta}$ . This latter result together with  $\mathbf{n}^{(R_N)} = \mathbf{R}_N \mathbf{n}$  gives  $\cos \theta^{(R_N)} = \cos(\theta + 2\pi/N)$  and  $\sin \theta^{(R_N)} = \sin(\theta + 2\pi/N)$ . As a consequence, Eqs. (1) and (2) are both satisfied at points rotated by a multiple of  $2\pi/N$  of a given orbit, with the same direction of motion, i.e.,  $\dot{\mathbf{r}}$  and  $\mathbf{n}$  rotated by  $2k\pi/N$ , as well as  $\theta$  translated by  $2k\pi/N$ , for  $k = 1, 2, \dots, N - 1$ . ■

As a consequence of Theorem C.2, either the orbit has the same symmetry or there are corresponding orbits rotated by multiples of  $2\pi/N$  with the same rotation direction. Therefore,  $\mathbf{R}_N$  operations on an orbit with the same  $N$ -fold rotational symmetry of the confining potential maps the orbit onto itself. Additionally, if the orbit does not have the same reflection symmetry of the potential, then Theorem C.1 asserts

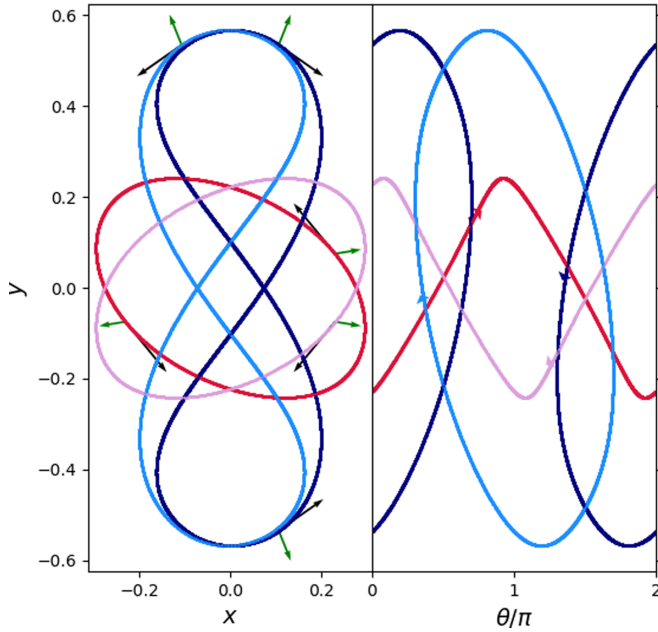


FIG. 10. Trajectories on the plane (left) and respective orientation angle versus  $y$  (right) for the elliptical confinement with  $\beta = 10$ ,  $\varepsilon = 1.0$ . The lighter (darker) colors depict (counter) clockwise rotations in the  $xy$  plane, whereas bluish (reddish) colors represent two(one)-loop orbits. Left: Dark arrows represent the particle velocity, while green arrows designate the gradient of the confinement potential. Right: Arrows indicate the direction of increasing  $\theta$ .

there should be an identical mirrored orbit rotating in the opposite sense, such as the orbits shown in Fig. 4(k), which have fourfold rotational symmetry but lack the same reflection symmetry of the potential. Other examples for confinements having dihedral symmetries are presented in Figs. 2(a)–2(d), as well as in Figs. 4(a)–4(d), 4(f), and 4(h).

To illustrate the implications of the theorems in more detail we examine two types of orbits (rotation and libration) in our elliptic confinement. This confinement has  $D_2$  dihedral symmetry, with two reflection symmetry lines, the horizontal and vertical axes, as well as twofold rotational symmetry. Therefore, we expect the particle trajectories to satisfy both theorems above.

In Fig. 10 we show the orbits projected on the  $xy$  plane (left panel) and  $y$  as function of  $\theta$  (right panel) of an active particle. Pink and red lines are mirrored orbits with  $|Q| = 1$ , while light and dark blue curves are mirrored orbits with  $Q = 0$ . In the left panel, the dark arrows depict the direction of motion. One can clearly see that they satisfy the requirements already mentioned for mirrored orbits. In the right panel, we see the inversion of  $\dot{\theta}$ , together with the shift of  $\pi$  for  $\theta$  of mirrored orbits, i.e.,  $\theta^{(S)} + \theta = \pi$  stated above.

Interestingly, reflection over the  $x$  axis furnishes mirrored orbits (red and pink curves) for these  $Q = 1$  case but a reflected part of the same orbit (blue and light blue curves) for the  $Q = 0$  case. Also, for each of the orbits in the latter case the inversion of motion above and below the  $x$  axis results in mirrored loops of opposite topological charges.

Furthermore, the twofold rotational symmetry manifest itself in orbits with  $|Q| = 1$ , since points along the orbit are

mapped on points rotated by  $\pi$  of the same orbit in the  $xy$  plane. On the other hand, orbits with  $Q = 0$  are mapped to their mirrored orbits in the  $xy$  plane. For  $Q = 0$  the rotational symmetry connects points along one orbit to points on the corresponding twin orbit. This mapping is the same as the one obtained by a reflection over the  $y$  axis followed by another reflection over the  $x$  axis.

Regarding the dependence on  $\theta$ , the reflection over the  $y$  axis and twofold rotation symmetries yield  $\theta^{(S_y)} + \theta = \pi$  and  $\theta^{(R_2)} = \theta + \pi$ , respectively. Therefore,  $\theta^{(S_y)} + \theta^{(R_2)} = 2\pi$ . In the right panel of Fig. 10, we see periodically continuous lines stretching from 0 to  $2\pi$  for the  $Q \neq 0$  orbits, which satisfy the above requirements. For the  $Q = 0$  cases these requirements result in alternate mirrored orbits in the  $\theta$ - $y$  plane.

Finally, these two types of orbits in the elliptical confinement illustrate the behavior that we observe for all the orbits obtained in different confinements. The requirements resulting from the symmetries, although do not necessarily impose restrictions on the particle trajectories, implicate in twin orbits which satisfy these requirements.

#### APPENDIX D: ANALYTICAL RESULTS FOR THE ELLIPTIC HARMONIC CONFINEMENT

For the results stated in this Appendix we consider the dimensionless forms of Eqs. (1) and (2) for the elliptic confinement given by Eq. (7).

##### 1. Area of closed loops

Here we demonstrate Eq. (9), which states that the oriented area of closed loops in a particle trajectory is proportional to  $\beta^{-1}$  for any orbit in the elliptic harmonic potential.

This can be seen by calculating the rate at which the oriented area  $A$  swept by the position vector of the particle changes over time,  $\frac{dA}{dt} = \frac{1}{2}(\mathbf{r} \times \mathbf{v}) \cdot \hat{z}$ . By noticing that  $\nabla V$  can be conveniently written in terms of the vectors  $\mathbf{r}$  and  $\bar{\mathbf{r}} \equiv (x, -y)$ , we rewrite Eq. (1) as

$$\mathbf{n} = \left[ \mathbf{v} + \left(1 + \frac{\varepsilon}{2}\right)\mathbf{r} + \frac{\varepsilon}{2}(x\hat{x} - y\hat{y}) \right]. \quad (\text{D1})$$

Substituting in Eq. (2) we find

$$(2 + \varepsilon)\frac{dA}{dt} = \frac{d}{dt} \left( \frac{\theta}{\beta} - \frac{\varepsilon}{2}xy \right). \quad (\text{D2})$$

Therefore,  $(2 + \varepsilon)A - \frac{\theta}{\beta} + \frac{\varepsilon}{2}xy$  remains invariant along any given orbit. By integrating (D2) along a single closed loop of the orbit, we find

$$A_{\text{loop}} = \frac{\Delta\theta_{\text{loop}}}{(2 + \varepsilon)\beta}, \quad (\text{D3})$$

where  $|\Delta\theta_{\text{loop}}| < 2\pi$  for any given loop of an orbit with nodes. In particular, for rotation orbits, one has  $A_{\text{orbit}} = \frac{2\pi}{(2 + \varepsilon)\beta}$ .

##### 2. Instability of orbital phase in the elliptic confinement

*Theorem D.1.* Orbital motion is not allowed in the elliptic confinement for  $\beta < 1$ .

*Proof.* To determine the region where orbital motion in the elliptic confinement cannot be stable we start rewriting Eq. (2) as  $\frac{d\hat{n}}{dt} = \beta[\mathbf{v} - (\hat{n} \cdot \mathbf{v})\hat{n}]$ , where  $\dot{\mathbf{r}} = \mathbf{v}$ . Multiplying it by  $\mathbf{v}$  we notice that  $v^2 = (\hat{n} \cdot \mathbf{v})^2 + \beta^{-1}(\mathbf{v} \cdot \frac{d\hat{n}}{dt})$ . Therefore, using Eq. (1),

$$0 \leq \left( \mathbf{v} \cdot \frac{d\hat{n}}{dt} \right) = \left[ \frac{1}{2} \frac{dv^2}{dt} + (\mathbf{v} \cdot \nabla)^2 V \right] \leq \beta v^2. \quad (\text{D4})$$

Since  $(\mathbf{v} \cdot \nabla)^2 V = v^2 + \varepsilon \dot{x}^2$ , we find

$$-(v^2 + \varepsilon \dot{x}^2) \leq \frac{1}{2} \frac{dv^2}{dt} \leq (\beta - 1)v^2 - \varepsilon \dot{x}^2. \quad (\text{D5})$$

As a consequence, for  $\beta < 1$ ,  $\frac{dv^2}{dt} < 0$  for any  $t$ . That means the particle velocity will eventually go to zero and orbital motion will not be sustained. Therefore, for  $\beta < 1$  orbital motion is not allowed in the elliptic confinement. ■

- 
- [1] B. Szabó, G. J. Szöllösi, B. Gönci, Z. Jurányi, D. Selmeczi, and T. Vicsek, Phase transition in the collective migration of tissue cells: Experiment and model, *Phys. Rev. E* **74**, 061908 (2006).
- [2] F. Giavazzi, M. Paoluzzi, M. Macchi, D. Bi, G. Scita, M. L. Manning, R. Cerbino, and M. C. Marchetti, Flocking transitions in confluent tissues, *Soft Matter* **14**, 3471 (2018).
- [3] E. Pinçe, S. K. Velu, A. Callegari, P. Elahi, S. Gigan, G. Volpe, and G. Volpe, Disorder-mediated crowd control in an active matter system, *Nat. Commun.* **7**, 10907 (2016).
- [4] D. Geyer, D. Martin, J. Tailleur, and D. Bartolo, Freezing a Flock: Motility-Induced Phase Separation in Polar Active Liquids, *Phys. Rev. X* **9**, 031043 (2019).
- [5] N. Kumar, H. Soni, S. Ramaswamy, and A. Sood, Flocking at a distance in active granular matter, *Nat. Commun.* **5**, 4688 (2014).
- [6] P. K. Bera and A. K. Sood, Motile dissenters disrupt the flocking of active granular matter, *Phys. Rev. E* **101**, 052615 (2020).
- [7] L. Giomi, N. Hawley-Weld, and L. Mahadevan, Swarming, swirling and stasis in sequestered bristle-bots, *Proc. R. Soc. A: Math., Phys. Eng. Sci.* **469**, 20120637 (2013).
- [8] C. Scholz, M. Engel, and T. Pöschel, Rotating robots move collectively and self-organize, *Nat. Commun.* **9**, 931 (2018).
- [9] A. Deblais, T. Barois, T. Guerin, P. H. Delville, R. Vaudaine, J. S. Lintuvuori, J. F. Boudet, J. C. Baret, and H. Kellay, Boundaries Control Collective Dynamics of Inertial Self-Propelled Robots, *Phys. Rev. Lett.* **120**, 188002 (2018).
- [10] M. C. Marchetti, J. F. Joanny, S. Ramaswamy, T. B. Liverpool, J. Prost, M. Rao, and R. A. Simha, Hydrodynamics of soft active matter, *Rev. Mod. Phys.* **85**, 1143 (2013).
- [11] C. Bechinger, R. Di Leonardo, H. Löwen, C. Reichhardt, G. Volpe, and G. Volpe, Active particles in complex and crowded environments, *Rev. Mod. Phys.* **88**, 045006 (2016).
- [12] L. Caprini, U. Marini Bettolo Marconi, and A. Puglisi, Spontaneous Velocity Alignment in Motility-Induced Phase Separation, *Phys. Rev. Lett.* **124**, 078001 (2020).
- [13] Y. Fily, A. Baskaran, and M. F. Hagan, Dynamics of self-propelled particles under strong confinement, *Soft Matter* **10**, 5609 (2014).
- [14] X. Yang, M. L. Manning, and M. C. Marchetti, Aggregation and segregation of confined active particles, *Soft Matter* **10**, 6477 (2014).
- [15] W. Yan and J. F. Brady, The force on a boundary in active matter, *J. Fluid Mech.* **785**, R1 (2015).
- [16] A. P. Solon, J. Stenhammar, R. Wittkowski, M. Kardar, Y. Kafri, M. E. Cates, and J. Tailleur, Pressure and Phase Equilibria in Interacting Active Brownian Spheres, *Phys. Rev. Lett.* **114**, 198301 (2015).
- [17] S. C. Takatori, R. De Dier, J. Vermant, and J. F. Brady, Acoustic trapping of active matter, *Nat. Commun.* **7**, 10694 (2016).
- [18] K. Malakar, A. Das, A. Kundu, K. V. Kumar, and A. Dhar, Steady state of an active brownian particle in a two-dimensional harmonic trap, *Phys. Rev. E* **101**, 022610 (2020).
- [19] I. Santra, U. Basu, and S. Sabhapandit, Direction reversing active brownian particle in a harmonic potential, *Soft Matter* **17**, 10108 (2021).
- [20] A. Geiseler, P. Hänggi, and G. Schmid, Kramers escape of a self-propelled particle, *Eur. Phys. J. B* **89**, 175 (2016).
- [21] E. Woillez, Y. Zhao, Y. Kafri, V. Lecomte, and J. Tailleur, Activated Escape of a Self-Propelled Particle from a Metastable State, *Phys. Rev. Lett.* **122**, 258001 (2019).
- [22] D. Wexler, N. Gov, K. O. Rasmussen, and G. Bel, Dynamics and escape of active particles in a harmonic trap, *Phys. Rev. Research* **2**, 013003 (2020).
- [23] S. Gu, T. Qian, H. Zhang, and X. Zhou, Stochastic dynamics of an active particle escaping from a potential well, *Chaos* **30**, 053133 (2020).
- [24] S. Perrard, M. Labousse, M. Miskin, E. Fort, and Y. Couder, Self-organization into quantized eigenstates of a classical wave-driven particle, *Nat. Commun.* **5**, 3219 (2014).
- [25] S. Jahanshahi, H. Löwen, and B. ten Hagen, Brownian motion of a circle swimmer in a harmonic trap, *Phys. Rev. E* **95**, 022606 (2017).
- [26] O. Dauchot and V. Démery, Dynamics of a Self-Propelled Particle in a Harmonic Trap, *Phys. Rev. Lett.* **122**, 068002 (2019).
- [27] M. Leoni, M. Paoluzzi, S. Eldeen, A. Estrada, L. Nguyen, M. Alexandrescu, K. Sherb, and W. W. Ahmed, Surfing and crawling macroscopic active particles under strong confinement: Inertial dynamics, *Phys. Rev. Research* **2**, 043299 (2020).
- [28] K.-D. N. T. Lam, M. Schindler, and O. Dauchot, Self-propelled hard disks: Implicit alignment and transition to collective motion, *New J. Phys.* **17**, 113056 (2015).
- [29] U. Basu, S. N. Majumdar, A. Rosso, and G. Schehr, Active brownian motion in two dimensions, *Phys. Rev. E* **98**, 062121 (2018).
- [30] S. Henkes, Y. Fily, and M. C. Marchetti, Active jamming: Self-propelled soft particles at high density, *Phys. Rev. E* **84**, 040301(R) (2011).
- [31] É. Fodor and M. C. Marchetti, The statistical physics of active matter: From self-catalytic colloids to living cells, *Physica A* **504**, 106 (2018).
- [32] C. A. Weber, T. Hanke, J. Deseigne, S. Léonard, O. Dauchot, E. Frey, and H. Chaté, Long-Range Ordering of Vibrated Polar Disks, *Phys. Rev. Lett.* **110**, 208001 (2013).

- [33] G. Briand, M. Schindler, and O. Dauchot, Spontaneously Flowing Crystal of Self-Propelled Particles, *Phys. Rev. Lett.* **120**, 208001 (2018).
- [34] D. Chaudhuri and A. Dhar, Active brownian particle in harmonic trap: Exact computation of moments, and re-entrant transition, *J. Stat. Mech.: Theory Exp.* (2021) 013207.
- [35] A. Wolf, J. B. Swift, H. L. Swinney, and J. A. Vastano, Determining lyapunov exponents from a time series, *Physica D* **16**, 285 (1985).
- [36] T. Tél, Y.-C. Lai, and M. Gruiz, Noise-induced chaos: A consequence of long deterministic transients, *Int. J. Bifurcat. Chaos* **18**, 509 (2008).
- [37] M. Iansiti, Q. Hu, R. M. Westervelt, and M. Tinkham, Noise and Chaos in a Fractal Basin Boundary Regime of a Josephson Junction, *Phys. Rev. Lett.* **55**, 746 (1985).
- [38] L. Ryashko and E. Slepukhina, Noise-induced torus bursting in the stochastic hindmarsh-rose neuron model, *Phys. Rev. E* **96**, 032212 (2017).
- [39] L. Billings, E. M. Bollt, and I. B. Schwartz, Phase-Space Transport of Stochastic Chaos in Population Dynamics of Virus Spread, *Phys. Rev. Lett.* **88**, 234101 (2002).
- [40] The basins of attraction of competing dynamical states were calculated as follows: We solved the deterministic version of Eqs. (1) and (2) starting from initial conditions distributed finely and uniformly in a volume of the phase diagram large enough to enclose the entire critical isoforce line and all orbits. The initial conditions are then classified according to the attractor to which they converge.
- [41] A. Pikovsky, Transition to synchrony in chiral active particles, *J. Phys.: Complex.* **2**, 025009 (2021).
- [42] I. S. Aranson and A. Pikovsky, Confinement and Collective Escape of Active Particles, *Phys. Rev. Lett.* **128**, 108001 (2022).
- [43] V. Makarenko and R. Llinás, Experimentally determined chaotic phase synchronization in a neuronal system, *Proc. Natl. Acad. Sci. USA* **95**, 15747 (1998).